IGC Newsletter

IN THIS ISSUE

Technical Articles

- Simple Insertable Variable Temperature Regulator for Physical Property Measurements at Low Temperatures

- The New Supercomputing Cluster

Young Officer's Forum

- An Approach Towards Design of Primary Sodium Pump for Commercial Breeder Reactor

Young Researcher's Forum

- High Pressure Phonon Analysis of $KMn[Ag(CN)_2]_3$ Single Crystals Studied by Raman Spectroscopy and First-Principles Calculations

Conference and Meeting Highlights

- DAE BRNS Theme Meeting on Plutonium 75

- 9th DAE-VIE (Vision for Information Exchange) 2016 Symposium on Emerging Trends in I&C and Computer Systems

Visit of Dignitaries

Awards & Honours

INDIRA GANDHI CENTRE FOR ATOMIC RESEARCH
http://www.igcar.gov.in/lis/nl109/igc109.pdf
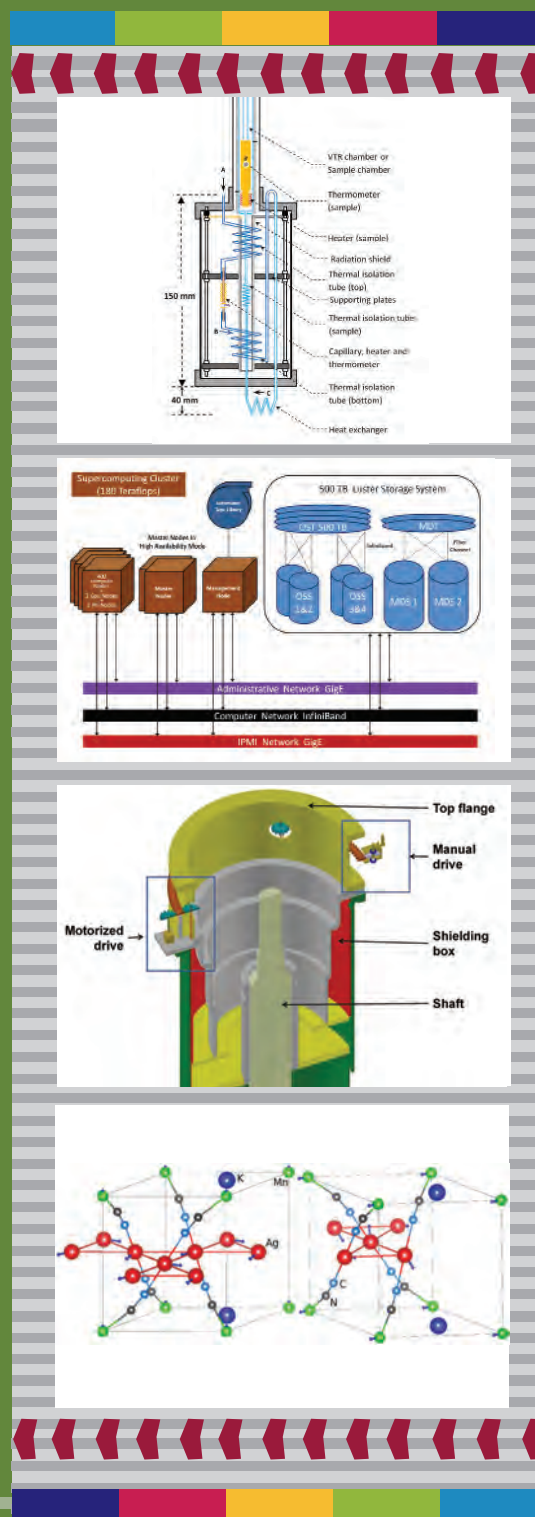
From the Editor

Dear Reader

This is the first issue being brought out after Dr. Arun Kumar Bhaduri has taken over as Director, IGCAR. It is my pleasant privilege to forward a copy of the latest issue of IGC Newsletter (Volume 109, July 2016, issue). In the first technical article, Dr. Nagendran and his colleagues describe the fabrication of a simple insertable variable temperature regulator and the evaluation of its performance.

In the second technical article Dr. Jayalal has elaborated on the recently commissioned multi-purpose parallel high-performance supercomputing cluster.

This issue's young officer's forum features an article by Shri Aravindan on the design of primary sodium pump for commercial breeder reactor.

Ms. Kamali has shared her experience on the high pressure phonon analysis on single crystals of $KMn[Ag(CN)_2]_3$ studied by Raman Spectroscopy and first-principles calculation in the young researcher's forum.

This Newsletter carries reports on the "DAE BRNS Theme Meeting on Plutonium 75" and 9th DAE-VIE (Vision for Information Exchange) 2016 Symposium on "Emerging Trends in I&C and Computer Systems".
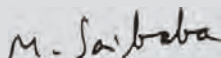
We had distinguished visitors to our Centre in the last quarter including Shri Vinod Kumar Thakral, IAS, Member (Finance), Atomic Energy, Space & Earth Commission and Dr. R. Chidambaram, Principal Scientific Advisor, Government of India.

We are happy to share with you the awards, honours and distinctions earned by our colleagues.

We look forward to your comments, continued guidance and support.

With my best wishes and personal regards,

Yours sincerely,

M. Saibaba

Chairman, Editorial Committee, IGC Newsletter

&

Associate Director, Resources Management Group

Our New Director

Dr. S. A. V. Satya Murty greets Dr. Arun Kumar Bhaduri on his assumption of charge as Director, IGCAR

Dr. Arun Kumar Bhaduri, Distinguished Scientist and Director, Metallurgy and Materials Group has taken over as Director, Indira Gandhi Centre for Atomic Research. He is from the 27th Batch of Training School and is a Homi Bhabha awardee. Dr. Arun Kumar Bhaduri is piloting the R&D programmes on the indigenous development of materials and fabrication technologies for sodium-cooled fast reactors, fusion reactors and advanced ultra supercritical thermal power plants. He has several research publications to his credit and is on the editorial board of several Journals. He is a recipient of the Humboldt Research Fellowship from the Alexander von Humboldt Foundation, Germany. He obtained his Doctorate from IIT Kharagpur and carried out post-doctoral research in University of Stuttgart, Germany.

Simple Insertable Variable Temperature Regulator for Physical Property Measurements at Low Temperatures

It is well known that most of the physical properties of materials such as electrical resistivity, AC magnetic susceptibility, DC magnetization, thermo-power, thermal conductivity etc. are temperature dependent and an accurate measurement of temperature dependence of such physical properties is important for inferring valuable information about elementary excitations in the system at a microscopic level. In order to carry out measurement of physical properties at low temperatures, it is necessary to design instruments, which enable one to vary and control the temperature of the sample under investigation with high temperature stability. Such an apparatus is usually called variable temperature regulator (VTR), and constitutes the central part of any physical property measurement system at low temperatures. In general, such measurements require the use of relatively expensive liquid helium as the cryogen and hence there is a need to minimize the overall consumption of liquid helium during the experiments. Different types of conventional VTRs such as exchange gas cooled, needle valve based and continuous flow cryostats have been conventionally used for varying the temperature of the sample from 4.2 to 300 K and vice versa. Each type of VTR, however, has its own advantages as well as disadvantages. In our laboratory, we had developed a novel impedance chamber based VTR, which has been incorporated in the SQUID magnetometer system for the study of temperature dependent magnetization of the sample under investigation. Indeed, the performance of this novel impedance chamber based VTR was found to be much superior to that offered by other conventional VTRs. This VTR design was based on the low viscosity of gaseous helium and its temperature dependence. The flow rate of the helium gas is inversely proportional to its viscosity and the viscosity of the helium gas increases with increase in temperature. The VTR comprises of an impedance chamber and VTR chamber (sample chamber enclosed within a thermal isolation chamber). The impedance chamber comprises of a fine capillary (optionally heated to the desired temperature) which acts as a control valve to adjust the flow of cold helium vapour into the VTR chamber. In this VTR design, it was necessary to provide two independent evacuation ports: one for the thermal isolation chamber and the other for the impedance chamber. The VTR, therefore, had to be designed in such a way that it is dedicated to a single experimental set-up such as the SQUID magnetometer and cannot be easily detached from this set-up for use elsewhere as desired by the user. A new design of a simple insertable VTR in which the VTR and the impedance chambers have been integrated together and share a common evacuation port is described. The simple insertable VTR may be used as a highly compact probe, which can be easily inserted either in a liquid helium storage dewar with a neck diameter of 50 mm or in a cryostat with a superconducting magnet with a clear bore diameter of 50 mm. Here we describe in detail the fabrication of this simple insertable VTR and the evaluation of its performance in terms of temperature stability, ability to achieve uniform rate of cooling/heating rate as desired by the user.

Principle of Operation of The Insertable Variable Temperature Regulator

The schematic view of the insertable VTR is shown in Figure 1. The liquid helium from the liquid helium reservoir (A) is drawn into a fine capillary (B) through a thermally isolated connecting tube. Here the liquid helium is converted into helium vapour using a heater and the helium vapor (say, between 15 and 25 K) is again cooled by a heat exchanger (C), located in the liquid helium reservoir, to a temperature near 4.2 K. This cold helium vapour is then drawn into the sample chamber by creating a differential pressure between the liquid helium reservoir and the sample chamber. The cold helium vapour serves as a refrigerant to cool the sample block or to maintain the sample block at constant temperature. Since the viscosity of the helium gas increases with increase in temperature, the volumetric flow rate of cold helium vapour through the narrow capillary tube decreases with increase in temperature. To control the flow rate, the fine capillary is heated using an electric heater. Therefore, the quantity of cold helium vapour drawn to cool the sample located in the sample block is very effectively controlled by the capillary acting as a fine control helium valve.

Fabrication

The liquid helium enters through a relatively wide capillary tube (ID ~1.2 mm) and its flow rate is restricted by allowing it to pass through a narrow stainless steel capillary tube with an inner diameter of 200 μm. An electric heater with a total resistance of 100 Ω has been wound over the fine capillary tube over a length of 50 mm using manganin wire of 0.1 mm diameter. A miniature Cernox thermometer has been mounted over the capillary just after the heater to monitor and control the temperature of the capillary. The electrical leads of the thermometer and heater are routed through the vacuum line (thermal isolation chamber) and terminated at the top of the insert with appropriate electrical feedthroughs. On both sides of the fine capillary tube, two connecting tubes (ID~1.2 mm) in the form of spiral coils (spiral diameter of 25 mm and spiral length of 30 mm) have been connected to reduce the thermal leak between the capillary tube and liquid helium reservoir by direct conduction. The whole arrangement is located inside a vacuum

chamber evacuated to a vacuum level better than 0.001 mbar. The outlet of the capillary is connected to the sample chamber by two connecting tubes with same inner diameter as used on both sides of the fine capillary again in the form of spiral coils. One coil,
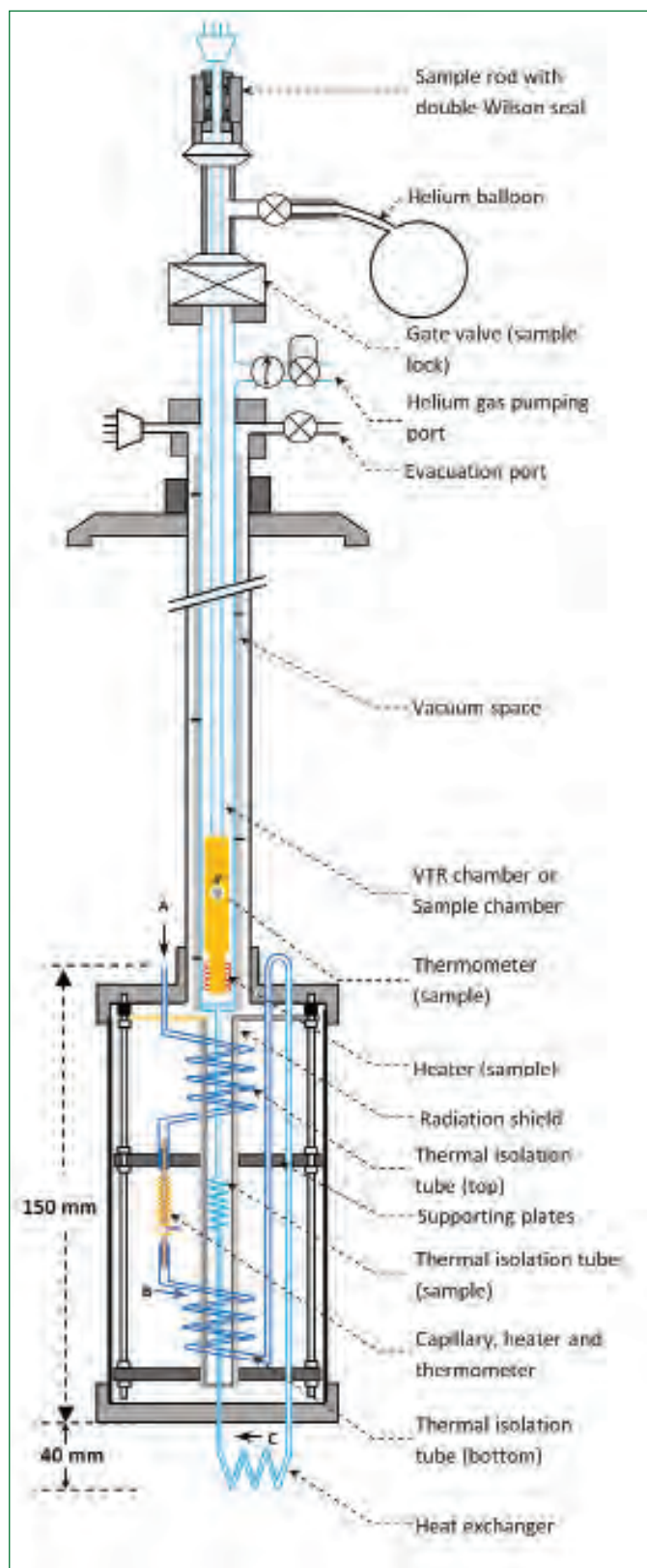

Figure 1: Cross sectional view of the insertable Variable Temperature Regulator (VTR)

which acts as a heat exchanger, is located inside the liquid helium reservoir and cools the incoming helium vapour from the heated capillary to a temperature close to 4.2 K. The other coil, also in the form of a spiral coil (with spiral diameter of 12 mm and length of 50 mm) is located at the centre of the vacuum chamber and thermally isolates the sample chamber from the liquid helium reservoir. The vacuum and sample chambers are combined and fabricated as a single unit using thin walled stainless steel tubes. The fine capillary tube and the other connecting tubes are made of stainless steel. The design and fabrication can be simplified by locating the heat exchanger tube at the place labeled as "C" in Figure 1. The sample chamber is fabricated out of thin walled stainless steel tube with its bottom end terminated in a sample block made of OFHC copper. The outer diameter of the OFHC copper block is about 10 mm. The sample under investigation can be loaded from the top of the insert through a valve, which acts as a sample lock. At the bottom end of the copper block, a heater with a resistance of $120\,\Omega$ has been wound by using manganin wire of 0.1 mm diameter. To measure and control the temperature in the vicinity of the sample region, a silicon diode thermometer has been mounted over the OFHC copper block. To maintain the differential pressure between the sample chamber and the liquid helium reservoir, pumping line has been provided at the top of the sample chamber.

Characterization

The performance of the VTR has been extensively investigated to evaluate the flow parameters to be controlled in order to achieve the desired uniform rate of cooling / heating as well as temperature stability. The VTR has been characterized in conjunction with a cryogenic temperature controller by operating it in the following different modes.

1. Cooling from 300 to 4.2 K, as well as heating from 4.2 to 300 K of the sample region with uniform rate of cooling and heating as desired by the user.

2. Maintaining temperature in the sample region constant for desired duration with high temperature stability.

(a) Uniform rate of cooling/heating

The rate of cooling can be maintained uniform throughout the temperature range from 300 to 4.2 K with the help of the temperature controller and by choosing appropriate values of the capillary temperature and the pressure in the sample chamber. The temperature controller is used to control both the capillary and sample temperatures to the desired value using independent feedback control loops. The user can set the desired cooling rate (K/min) and appropriate heater power in the temperature controller. The capillary temperature and the sample chamber pressure can then be automatically chosen by the custom-designed software easily set using the cryogenic temperature controller and the
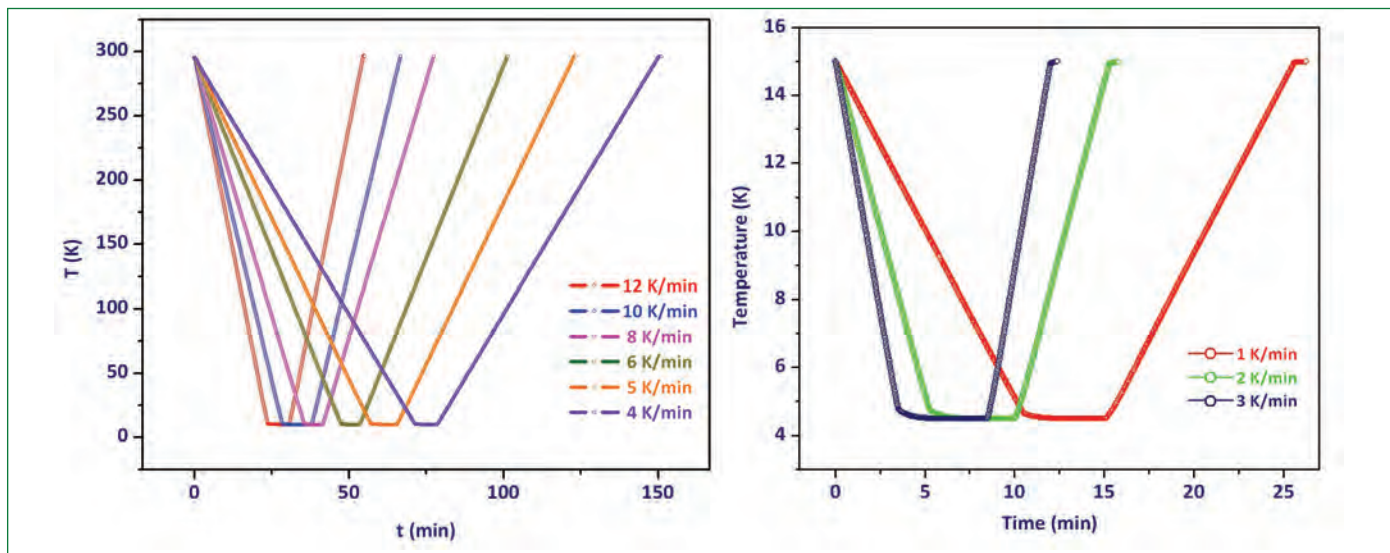
Figure 2: Variation of the temperature in the vicinity of the sample for different uniform controlled cooling and heating rates (a) 4 to 12 K/min and (b) 1 to 3 K/min

pressure controller, respectively in order to achieve the desired sample cooling rate). Figure 2 shows the control in the variation of the temperature in the vicinity of the sample region for different values of selected cooling and heating rates. It is evident from the figure that the present VTR enables cooling and heating of the sample at a uniform rate as desired by the user.

(b) Temperature Stability

In the other mode, the temperature of the sample region can be maintained constant at any desired temperature, starting from a temperature, which may be either above or below the desired temperature. If the desired temperature is above the current temperature (requiring heating), the capillary temperature has to be set to a temperature above 26 K to restrict the volume and flow rate of cold helium vapour through the capillary. On the other hand, if the desired temperature is below the current temperature (requiring cooling), the capillary temperature has to be set to about 22 K. Excellent temperature stability better than $\pm$ 1 mK has been successfully demonstrated using this insertable VTR over a wide temperature range from 4.2 to 295 K. As an illustration of the temperature stability, achieved experimentally using the present VTR, Figure 3 shows the temperature stability while maintaining the sample region at different constant temperatures of 100, 200 and 295 K. The time taken to stabilize the set temperature is only about 3 to 4 minutes after reaching the target temperature even when the difference between the current temperature and the set temperature is about 100 K, with a ramp rate set at 5 K/min. It is also observed that, while maintaining the temperature of the capillary above 26 K, the temperature stability of the sample region is excellent which is due to the fact that small amount of cold gaseous helium available from the capillary is sufficient to stabilize the temperature in the sample region and hence the use of heater power is minimal.

(c) Liquid helium consumption

The major sources responsible for the consumption of liquid helium are listed below.

i) Liquid helium flows through the capillary and this flow varies with change in the temperature of the capillary. During the
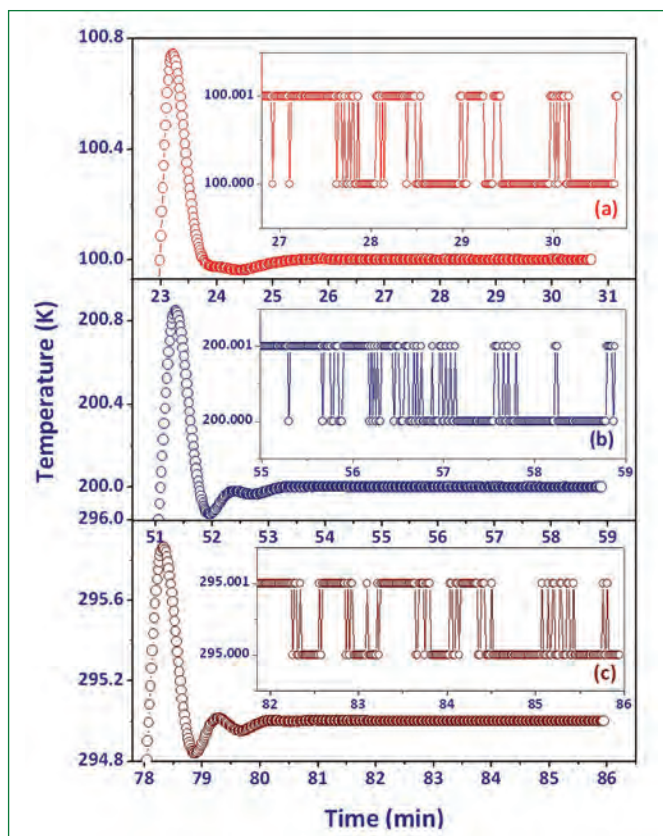

Figure 3: Temperature stabilities recorded experimentally while maintaining a constant temperature of (a) 100 K (b) 200 K and (c) 295 K in the vicinity of the sample region
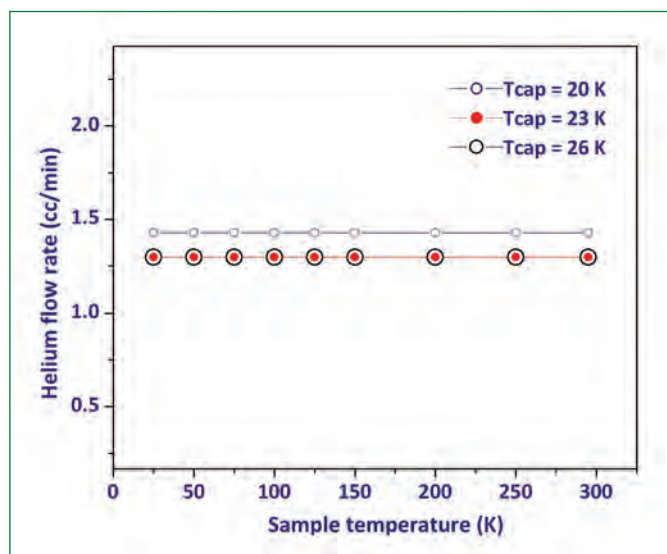
Figure 4: Liquid helium consumption through the capillary for different capillary temperatures and for different sample temperatures

Figure 5: Liquid helium consumption recorded at the outlet of the dewar for different capillary temperatures and for different sample temperatures

operation of the VTR, liquid helium evaporates in the dewar due to heat leak from the connecting tubes (thermal isolation tube (Top) and thermal isolation tube (bottom) in Figure 1) on both sides of the capillary; this heat leak varies with the capillary temperature.

ii) Liquid helium in the dewar evaporates due to heat leak from the sample chamber through the connecting tube (thermal isolation tube (sample chamber) in Figure 1.

The consumption rate of liquid helium have been independently recorded using two helium gas flow meters fixed at the exit of the sample chamber of the VTR and the outlet of the liquid helium dewar. The flow meter readings have been recorded at the outlet of the sample chamber (outlet of the pump) for different constant sample temperature (say 25, 50 K, etc.) by maintaining the capillary temperature constant at 20 K. These experiments have been repeated for the capillary temperature of 23 K. From Figure 4, it is observed that liquid helium consumption rate is independent of sample temperature and decreases with increase in the temperature of the capillary.

Simultaneously the flow meter readings have been recorded at the outlet of the liquid helium dewar for different sample temperatures (say 25, 50 K, etc.) by maintaining the capillary temperature constant at 20 K. These experiments have been repeated for the capillary temperatures of 23 and 26 K. From Figure 5, it is observed that the liquid helium evaporation rate increases with an increase in capillary temperature; this is on account of the heat leak through thermal isolation tubes connected on both sides of the capillary. It is also observed that the major heat leak to helium reservoir is due to the thermal isolation tube (sample chamber) located between the sample and liquid helium reservoir. Since the evaporation rate is found to significantly increase only when the
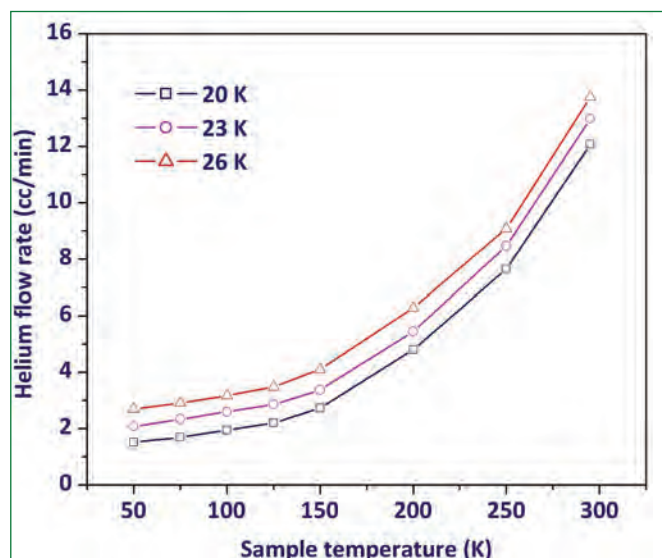
sample temperature exceeds 150 to 200 K, this may be due to the heat leak by thermal conduction from the sample chamber to the liquid helium reservoir through the thermal isolation tube or heat leak due to thermal radiation between the sample chamber and liquid helium reservoir. This heat leak due to thermal radiation can be reduced by adding additional layers of aluminized mylar sheets in the space available in the thermal isolation chamber.

The simple insertable variable temperature regulator suitable for use in liquid helium dewar with a neck diameter 50 mm or in a cryostat with a superconducting magnet with a bore diameter of 50 mm has been designed, fabricated and characterized extensively. Uniform rate of cooling/heating of the sample region from 1 to 12 K/min has been achieved by setting optimum flow parameters such as capillary temperature and pressure in the sample chamber with help of temperature and pressure controllers. When we compare the performance of the VTR with the other VTRs such as exchange gas cooled VTR and continuous flow cryostats, the heating/cooling of the sample region at a uniform rate is almost impossible in the case of exchange gas cooled VTR and the consumption of liquid helium to cool the sample space from 300 to 4.2 K is very high (about 3 to 4 liters) in the case of continuous flow cryostats. Excellent temperature stability of $\pm$ 0.001 K has been achieved using this VTR over a wide temperature range between 4.2 to 295 K which cannot be readily achieved in both exchange gas cooled VTR and continuous flow cryostats. In view of the excellent performance of the VTR, it can be used in any low temperature measurement system requiring fast and economic cooldown and excellent temperature control.

Reported by
R. Nagendran & Colleagues
Materials Science Group

The New Supercomputing Cluster

High-performance, supercomputing cluster systems have become widely accepted and cost effective solution for building supercomputers. In addition, the computing cluster concept offers better performance and availability over that of a single supercomputer. Convergence of a number of technological advances in computing, including the availability of low-cost microprocessors, high-speed networks and software for distributed computing has led to the emergence of computing cluster systems. They have got a wide range of applicability and deployment, ranging from small business clusters with a handful of nodes to some of the fastest supercomputers such as Tianhe-2 (the second fastest supercomputer in the world). High-performance computing is revolutionizing the speed and efficiency of scientific research and development at a very fast pace. It has been recognized by the scientific community that integrating high-performance computing to mathematical modeling, numerical algorithms and large scale data bases, would lead to a new paradigm in science and engineering. At large, high performance computing offers solutions to the large-scale computational requirement of mathematical modelling and computational simulation studies.

Recently, a multi-purpose parallel high-performance computing cluster delivering a sustained numerical performance of 180 Teraflops has been installed and commissioned. The cluster is designed to meet the large scale numerical and data intensive computing requirements of the organization. With the commissioning of the supercomputing cluster, the cumulative high performance computing power at the Centre crosses the 200 Teraflops mark. The front side view of the new cluster system is given in Figure 1. The details of the configuration and salient features of the system are given below.

Configuration of the Cluster

The system has two master/login nodes and four hundred compute nodes, along with two additional compute nodes with Graphics Processing Unit (GPU) accelerators and two nodes with Intel Phi coprocessors. The master node is the head node of the cluster, which is used for cluster administration and also provides user interface for job submission and management. In order to increase the availability of the cluster, the node is configured in high-availability mode. In addition to the master node, a management node is also configured for the hardware management of all the compute nodes. The compute nodes are the cluster nodes where the users' jobs actually run. They are highly optimized to execute the parallel codes of the users. Each compute node has dual, 12-core 64-bit Intel Xeon Ivy-bridge processors and 128 Gigabytes of primary memory. The compute nodes offer a total of 9600 processor cores and 52 Terabytes of primary memory. The Graphics Processing Unit node has two NVIDIA Tesla K40 GPUs and the Phi Node is based on two Intel Phi 7120P coprocessors. The overall configuration of the system is given in Figure 2, depicting the major functional units and the inter-connections.

Interconnect Networks

In order to exploit the full potential of the supercomputing cluster and its high processor speeds, interconnects between the cluster nodes are essential. The cluster system has three interconnect networks. The primary network meant for inter-process communication is based on the *InfiniBand architecture.* InfiniBand is an industry standard, channel-based, switched fabric, interconnect architecture for servers. It provides very high bandwidth and low latency for communication and better scalability. It uses low-level Remote Direct Memory Access (RDMA) protocol to reduce the application latency and processor overhead. The *InfiniBand* switch supports up to 648, high data rate ports each with a bandwidth of 56 Gbps. The switch is with comprehensive chassis management and fabric management features and offers 72.5 Terabits per second switching capacity. The other two networks are based on Gigabit Ethernet and are meant for administration and hardware remote management respectively. The hardware remote management network provides remote access, monitoring and control functions for cluster nodes, without using additional switches and complex wiring. This network utilizes the Intelligent Platform Management Interface (IPMI) technology that is

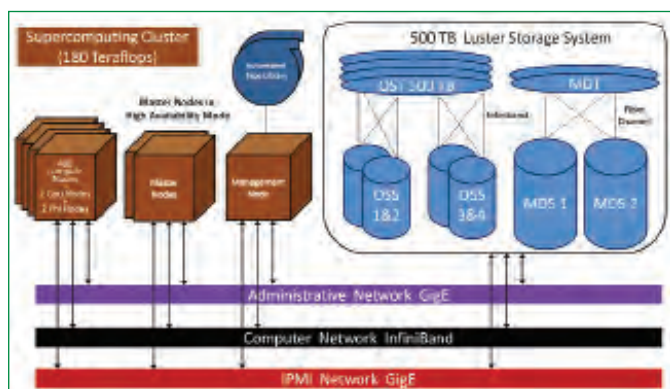Figure 1: The front side view of the new supercomputing cluster

Figure 2: The overall configuration of the supercomputing cluster depicting the major functional units and the inter-connections

supported by Intel.

Storage System

The storage system of a high-performance computing cluster needs a large capacity of storage, accessible at high speeds in high availability mode. Simultaneous access from multiple nodes and a single global names pace are the two other requirements for the storage. In order to meet these requirements, the storage system of the cluster is configured using a parallel and distributed file system named as Lustre. Lustre is an open-source file system and supports all the special requirements of storage of the cluster system.

The Lustre storage architecture consists of two metadata servers (MDS) which manage the names and directories in the file system and four object storage servers (OSS) which provide file input/output (I/O) service. Lustre metadata servers are configured in active/passive mode, while object storage servers are deployed in active/active mode. This configuration provides redundancy without extra overhead that improves file system performance, enhances file system recover ability and availability. The recovery feature of Lustre, allows servers to be upgraded without the need to take the system down. The hard disks in storage units are configured in RAID level 6, enabling file system operations to continue in the event of a double disk failure. The object storage servers are connected to storage units using InifiniBand links and metadata servers are connected to meta-data storage units using fiber-channel links. The data backup requirements of the cluster are fulfilled with an automated tape library consisting of four, Linear Tape-Open (LTO-6) tape drives and 120 tape slots, attached directly to the management node. The backup software is configured in the management node to take periodic backups of user data.

Cooling and other Features

The whole system is housed in fourteen, standard height (42U) server racks which are arranged in two rows, each with seven racks. The industry-leading cooling concept named Rear Door Heat Exchanger (RDHx), that uses chilled water to provide cooling for individual racks, is installed. The RDHx device, which resembles an automobile radiator, is placed in the airflow outlet of the rack, by replacing the standard rear doors. During operation, the rack's hot airflow is forced through the RDHx device by the fans of the cluster nodes. Heat is exchanged from the hot air to water circulating from the Cooler Distribution Units (CDU). This cooling solution utilizes the better heat removal capacity of water over air and provides significant advantages over traditional air cooling systems, like better efficiency, simple design and noiseless operation.

The electrical requirement of the supercomputing cluster is estimated as 200 KVA. Uninterrupted power supplies (UPS) and diesel generator backup are provided to some of the critical systems, like master nodes, storage system, InfiniBand switch and management node. The facility has equipped intelligent smoke and heat detectors with dual optical & heat sensors. The detection parameters of these sensors are set at most sensitive level.

Advanced cluster distribution software named Ganana is used for building and managing the software modules of the cluster. The cluster nodes run on open source, 64-bitLinux operating system and installed with latest version of Intel C/C++and FORTRAN compilers. Several scientific and mathematical libraries and special-purpose engineering applications have been installed. For cluster management and job scheduling, an open source, fault-tolerant and highly scalable software tool named "Slurm" has been installed.

Performance Benchmarking

The performance of the cluster is measured in terms of number of floating-point operations per second (Gigaflops/Teraflops). The industry-standard High-Performance Linpack (HPL) was used to evaluate the performance of the supercomputing cluster. It was found that the system gives a sustained performance of 180 Teraflops. The maximal sustained performance could be achieved after fine-tuning various system factors and benchmarking parameters. Currently the cluster system is one of the fastest supercomputing cluster available in the Department. Based on the sustained performance ratings, the cluster could be rated in the top twelve supercomputers in India.

Applications

This parallel supercomputing cluster is designed to meet the large-scale numerical computing requirements of scientists and engineers of IGCAR. Highly compute-intensive scientific applications in the areas of Computational Molecular Dynamics, Material design with desirable properties, Reactor Core calculations, Multi-scale modeling of radiation damage, Quantum Monte Carlo investigation of materials, Computational modeling and simulations of Plutonium recovery, Weather modeling and Engineering applications in the area of Finite Element Analysis, Computational Fluid Dynamics can effectively make use of the cluster to vastly reduce their run times.

M. L. Jayalal & Colleagues
Electronics and Instrumentation Group

Young Officer's FORUM

An Approach Towards Design of Primary Sodium Pump for Commercial Breeder Reactor

Shri S. Aravindan is working as Scientific Officer in Sodium Circuits Section of Reactor Design Group. He is from 11th batch of DGFS, and obtained his B.E degree (Mechanical Engineering) from PSG College of Technology, Tamil Nadu in 2012 and M.Tech in Machine Design from IIT Madras in 2014. His current area of work comprises of designing and testing the flow blockage devices and other components of the sodium pumps for future FBRs.

Commercial Breeder Reactor (CBR) of 600 MWe is conceptualized with a focus on safety, economy and breeding. CBR, with three primary sodium pumps (PSP), is envisaged to have 20% higher power than 500 MWe Prototype Fast Breeder Reactor (PFBR), which has only two PSP. A schematic of PSP of CBR is shown in Figure 1. PSP, being a dynamic component in the primary sodium circuit, requires a pragmatic design approach to ensure its trouble free operation under various possible scenarios. Testing of PSP of
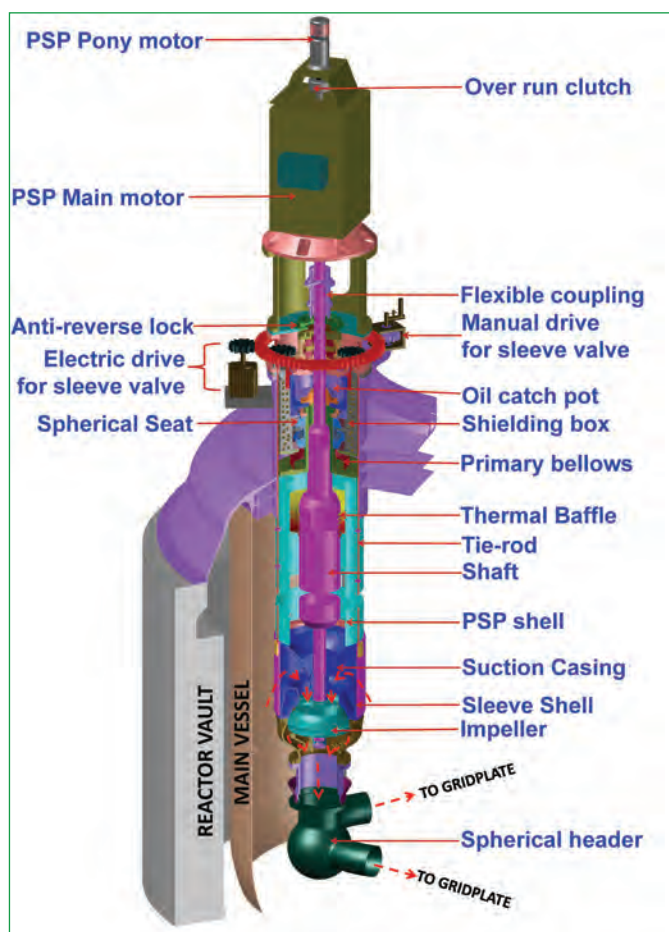

Figure 1: Schematic on PSP of CBR

PFBR provided critical feedback on its performance. Stretching the limits of various parameters like impeller diameter, suction speed and operating speed of PSP of PFBR had resulted in technical difficulties during technology development, testing, etc., which were successfully resolved with a meticulous approach. Hence, in the design of PSP of CBR, considerable importance is given for the manufacture and testing experience of PSP of PFBR. It is observed that, if two pumps are used for CBR, the suction energy is further increased compared to that of PFBR's PSP, resulting in increased chances of cavitation, erosion, and other associated difficulties. Further, giving due importance to the life of PSP impeller to twenty years, three pumps are finalized for primary sodium circuit in CBR. The other advantages with the choice of three PSPs are

i. Net Positive Suction Head Required ($NPSHR_{3\%}$) for each pump will reduce as the flow per pump decreases. This provides sufficient margin to avoid cavitation.

ii. Provides operational flexibility for the reactor during startup if one out of three PSP is not available (2/3 mode), thereby enhancing plant availability.

iii. Since flow handled per pump is reduced compared to PFBR, the overall diameter of PSP will be less.

iv. Cost involved in technology development of large-sized components will reduce.

Head and Flow Requirements

Flow rating of PSP was arrived from three major considerations namely (i) core flow, (ii) various bypass flow and (iii) main vessel cooling flow requirements. The core flow requirement is estimated to be 7900 kg/s, which is 22.6% higher than PFBR. The major bypass flow paths in PFBR are through Eddy current flow meter, hydrostatic bearing, pump-pipe connection, grid plate sleeve and inter-wrapper space. Due to welded grid plate design, leakage through grid plate sleeve bypass is reduced to zero for CBR. The number of sub-assemblies (SA) with inter-wrapper flow is reduced
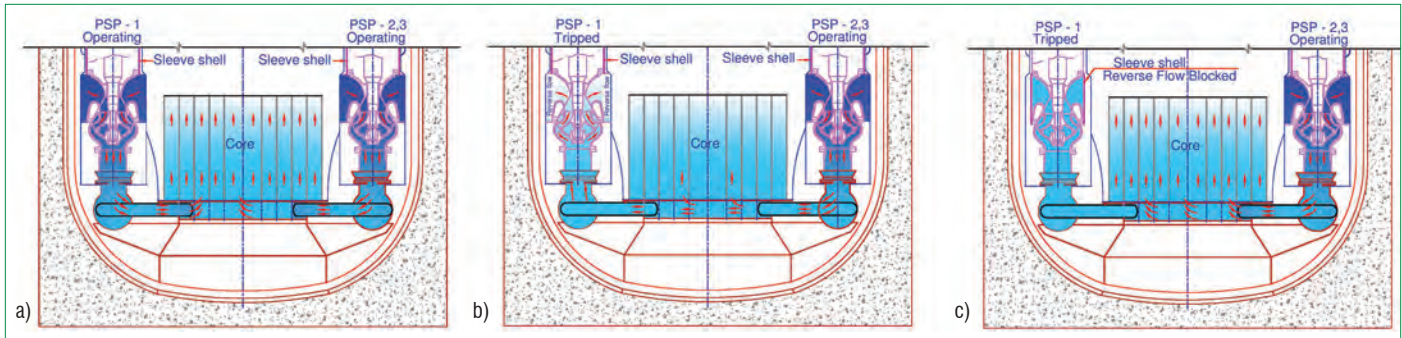
Figure 2: Flow pattern in the reactor when (a) all PSP are operating normally (b) after a PSP trip (c) after the closure of tripped pump's suction by sleeve valve

in CBR. Thermal hydraulic studies have indicated reduction in main vessel cooling requirements. Overall, in terms of bypass flow per MWth, there is a 33.4% reduction in CBR as compared to PFBR.

The major portion of head supplied by PSP is to overcome core resistance (86% of the total head). Remaining pressure drop occurs in other components namely header, primary pipe, grid plate, IHX and entry losses to the pump. An increase in pressure drop in IHX is accommodated in the existing margin available, and the head requirement is maintained as 75mlc as in PFBR.

Flexibility in the operation of PSP can increase the availability of plant and hence higher capacity factors can be achieved. In PFBR, tripping of one out of two PSPs will lead to the trip of reactor i.e., for power operation, both PSPs must be operational. Whereas, in the case of CBR if one of the PSP trips, operation of the reactor with two PSPs (2/3 mode) improves plant availability. In the event of operation in 2/3 mode, a significant portion of pumped flow would flow through the tripped (idle) PSP, which offers the least resistant path for sodium flow compared to the core as shown in Figure 2b. If the flow path through the tripped PSP is made highly resistant as compared to the core, then eventually, flow from the two operating PSPs will go through the core as shown in Figure 2c. Such a flow blocking/resisting arrangement can also provide the flexibility of commissioning the pump individually during reactor start-up.

To prevent flow reversal, non-return valves were considered for PFBR in the 1980s. However, the non-return valves are not provided, as the reactor is not envisaged to operate with single primary pump. With three pumps in CBR, power operation with two pumps can provide operational flexibility. Hence, there is a need for a simple and reliable flow blocking device. Therefore, the flow blocking arrangement has to be custom designed for PSP. A conceptual design of a flow blocking arrangement is studied with considerations on ease of operation, location of blocking, drive arrangements, etc. A cylindrical shell (sleeve shell) is designed to close the suction passage of the tripped PSP, thereby making the path highly resistant for reverse flow. However, since the suction passage is located in the lower region of the PSP, sleeve shell needs

to be operated from over the roof slab with the help of manual/motorized drive. To achieve this tie-rods are utilized for connecting the drive and sleeve shell.

Sleeve Valve Mechanism

The sleeve shell is designed considering various normal/off-normal conditions of head and flow rate encountered during operation of sleeve valve. A typical system-pump characteristic curve is shown in Figure 3. Let, P1 be the operating point at design speed 'N', where all three PSPs are working. When one PSP trips, the operating point will shift momentarily to P2, which is of lower head and flow rate compared to P1. Since the tripped pump acts as major leak path (bypass) for the sodium pumped by other two working PSPs, the system curve changes and hence operating point shifts to point P3, which has a lower head but higher flow rate per pump compared to P1. Since the higher flow rates at a lower head of operation are not recommended from cavitation consideration, the speeds of other two PSPs are reduced, and a new operating point P4 is attained. At this point, when the reverse flow is blocked with the sleeve shell the operating point will become P5. Then, the majority of pumped flow will pass through the core. Then the speed of other two PSPs can be increased for power operation of the reactor.
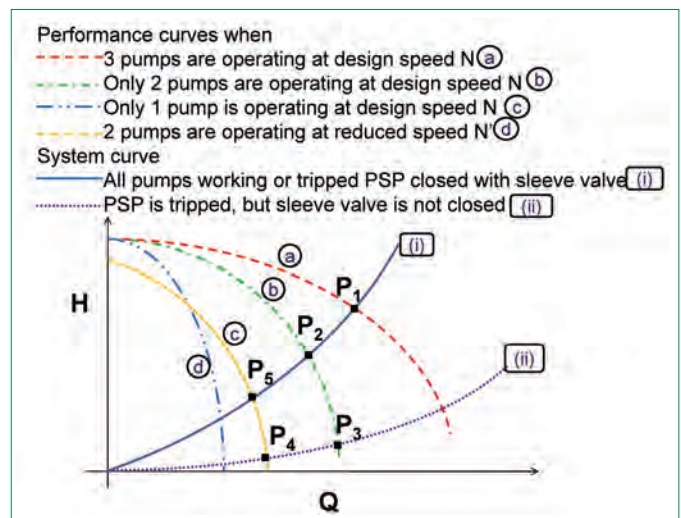

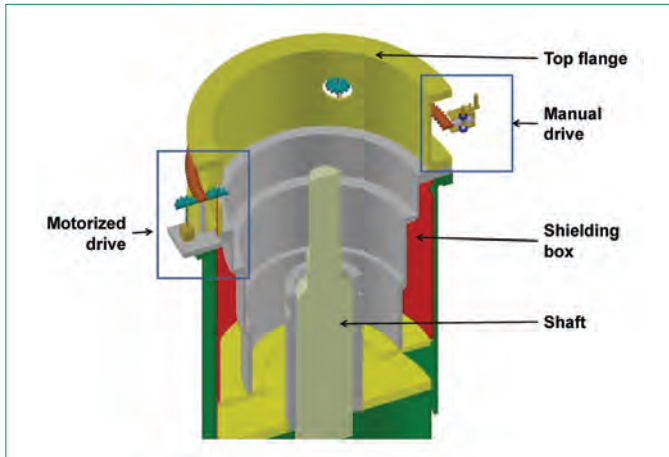Figure 3: Operating points of pump under different scenarios

Figure 4: Manual and motorized drive for the movement of sleeve shell

Figure 5: Leakage through the closed sleeve shell

Three tie-rods are incorporated for raising or lowering the sleeve valve, and the synchronized movement of the tie-rods is achieved with the help of an annular gear, which will be driven by a motor. Along with the motorized drive, a provision for manual operation is considered with the addition of a simple gear system as shown in Figure 4. Since the mechanism is driven by a single drive motor, spurious signal to the motor can result in closing the sleeve valve when the pump is operating, leading to suction throttling, which has to be avoided. Hence, to avoid such scenarios, an interlock is incorporated.

When the sleeve valve is closed, there will be an annular gap between the sleeve shell and the PSP shell as shown in Figure 5. This gap cannot be made zero as the clearances are essential for relative movement between them. Hence, it is essential to estimate the leakage through this annular gap and the velocity of flow. Pump characteristics are developed theoretically, and system curves are plotted with leak path present. It was found that leakages are 6.9 and 1.9 % for a diametrical clearance of 9 and 3 mm. However, leak velocities are about 20 m/s, which is not permissible. Hence, a labyrinth is provided along the leak path; clearances are reduced
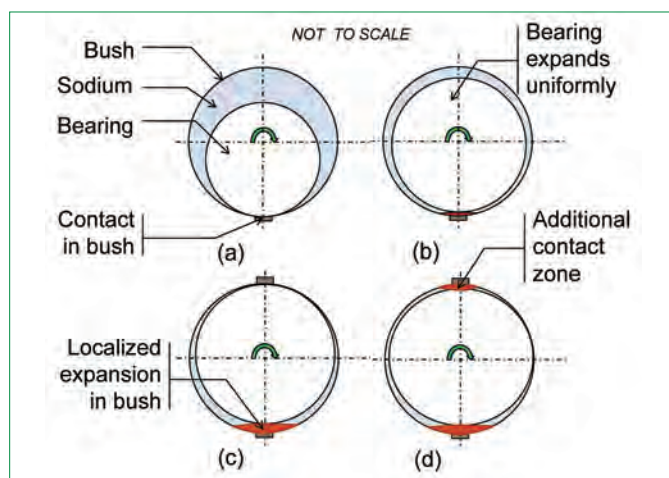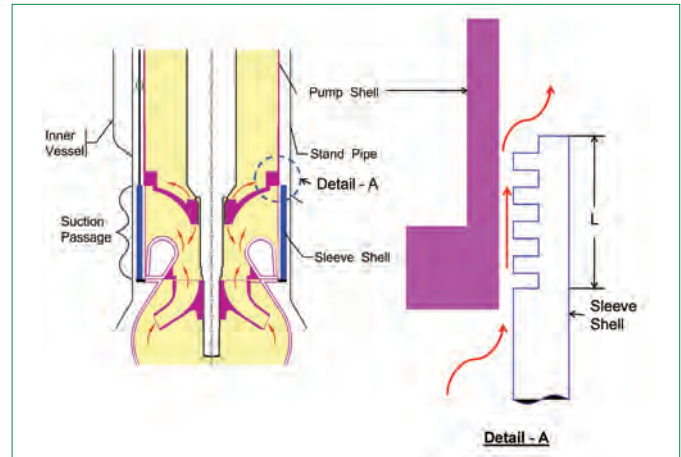
and optimization of parameters of labyrinth results in a reduction of leakage to 1.6 and 0.7% during maximum and minimum clearance conditions, respectively. Further, the leak velocities were reduced to the order of 10 m/s.

Seizure

Safety studies related with the finalization of shutdown system calls for an analysis of two PSP seizure as design extension conditions (DEC) with the seizure time considered as ≤ 1sec. Seizure of PSP occurs at hydrostatic bearing (HSB), where the clearances were reduced to zero due to various grounds like the inclusion of particulate matter, non-uniform thermal expansion, etc., thereby resulting in an increase in frictional torque when the shaft will come to rest. This is considered as a seizure event.

The mechanism of seizure is modelled mathematically to estimate seizure time. It is assumed that bearing is rotating at a constant speed, and the contact point on bush remains unchanged as shown in Figure 6a. Based on the speed of the shaft, sodium flow is assumed in the HSB clearance. The heat generated due to friction is estimated based on speed and it is distributed evenly between the contact area in bearing and bush. The frictional heat increases the temperature of both bearing and bush, which causes localized expansion in the bush as shown in Figure 6b and Figure 6c. However, the expansion is uniform in bearing as the shaft is rotating and a portion of heat is dissipated to the sodium. The study revealed that temperature rise in the shaft is marginal. However, the expansion in bush introduces additional contact on top of the bush as shown in Figure 6c, reducing the clearance to zero. Further increase in thermal expansion results in additional contact zone as shown in Figure 6d, which resists the rotation, thereby increasing the frictional torque and resulting in shaft seizure.

It is found that seizure time (time from initial contact to complete seizure), with simultaneous failure of over current trip (trip 1) and mechanical trip (trip 2), when the flywheel is mounted on pump

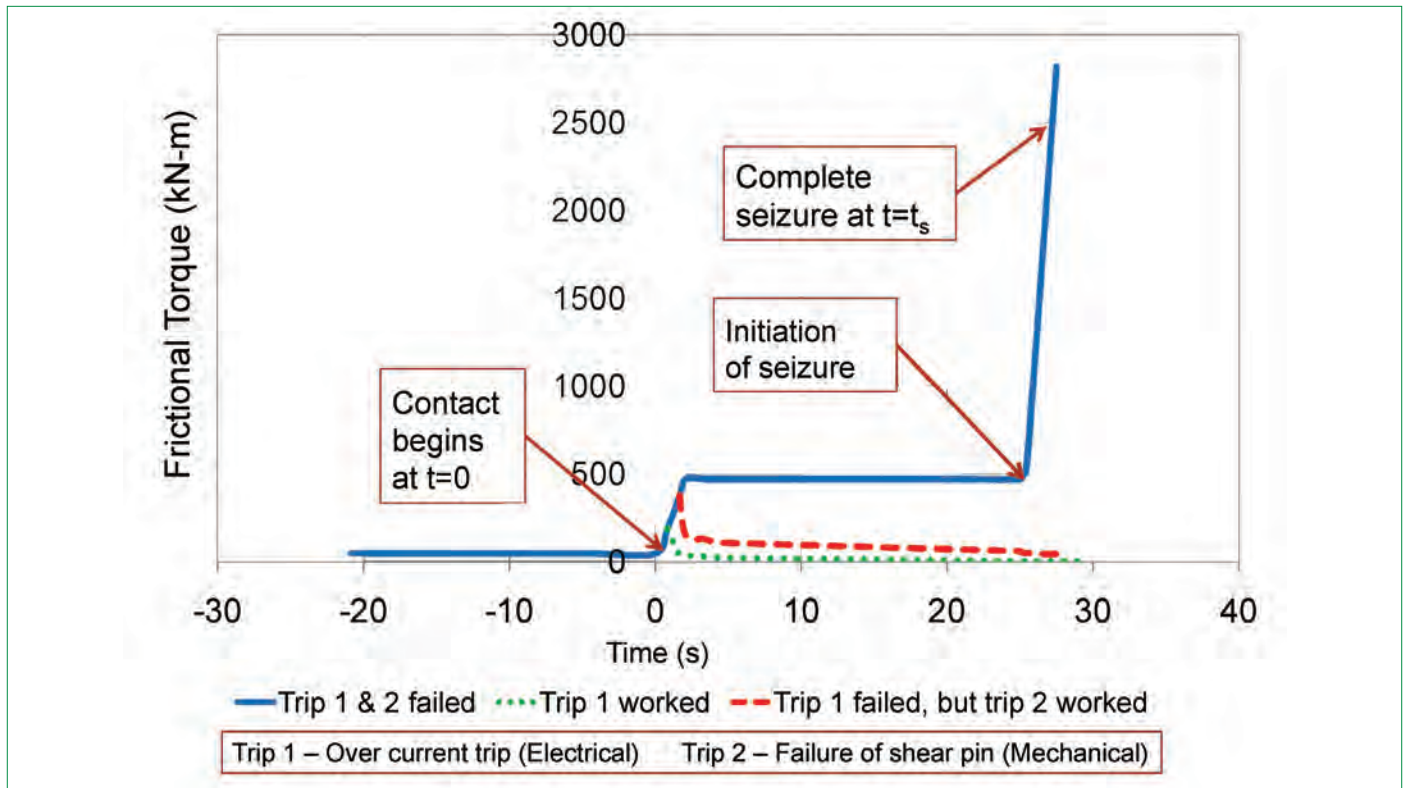Figure 6: Visualization of mechanism of seizure

Figure 7: Frictional torque and seizure time at HSB under various circumstances

shaft, under SSE loading conditions, is found to be 24 seconds as shown in Figure 7. On the other hand, if the flywheel is provided on the motor shaft, seizure time increases by 148 % to 62 seconds, due to decrease in radial loads at HSB. However, in the event of either one of the trips (trip 1 or trip 2) works, then the speed will reduce and the seizure time will phenomenally increase beyond 62 seconds.

Flow Coast Down Requirements

A flywheel is incorporated for providing flow coast down in pumps; thereby instantaneous loss of flow through the core will be avoided. In the design of PSP of PFBR, the flywheel is provided on the motor shaft instead of the pump shaft, as the flywheel's inertia will result in catastrophic failure of the pump shaft, if seizure occurs. The motor shaft is connected with the pump shaft through a flexible coupling. The flexible coupling contains a shear pin, which will fail (if the motor fails to trip due to over current) when the pump shaft encounters higher frictional torque (due to seizure), thereby disconnecting the flywheel from pump shaft. Hence, failure of shear pin results in loss of pump coast down phenomena. However, shear pin (mechanical trip) cannot be removed as it will bring sole reliance of the pump trip only on electrical parameters.

Flywheel, if present on pump shaft, will be able to satisfy flow halving requirements. Studies were carried out to investigate the feasibilities of providing flywheel on the pump shaft. Literature and analytical studies showed that the seizure is not instantaneous as widely assumed. Hence, the choice of the flywheel on pump shaft can be considered.

With the addition of the flywheel, which is heavier than the pump shaft, the loading on thrust bearings will increase. The seals have to be designed to withstand higher torque values. Though above constraints can be addressed by design modifications, balancing of the shaft with impeller and flywheel will be a tremendous task due to the overhung nature of flywheel. Gyroscopic forces will increase due to overhung flywheel and pump's angular inclination will increase. Hence alternative designs are being worked out, weighing their pros and cons to ensure and meet flow coast down under all possible scenarios.

With the margins available in the design of PSP for CBR, optimization of parameters (e.g., size, weight, cost, etc.) of the PSP is possible. With the provision of new features like the sleeve valve mechanism as mentioned above, the flexibility in the operation of PSP is improved thereby increasing the plant availability. Improvements in the existing system are done to enhance safety, reliability and economics of operation. Operating experience of PSP of PFBR can provide further insight into design modifications and new features required by PSPs. Full-scale water testing of PSP of CBR and testing of sleeve valve operating mechanism are also being planned as a part of future R&D.

Reported by
Aravindan & Colleagues
Reactor Design Group

Young Researcher's FORUM

High Pressure Phonon Analysis of KMn[Ag(CN)$_2$]$_3$ Single Crystals Studied by Raman Spectroscopy and First-Principles Calculations

Ms. K. Kamali did her Masters in Chemistry from Kanchi Mamunivar College, Pondicherry. She joined IGCAR as a Junior Research Fellow in Chemical Science in August 2010 and carried out her doctoral work in the Materials Science Group, under the guidance of Dr. T. R. Ravindran. Her doctoral thesis is on "High pressure Raman spectroscopic studies on anomalous thermal expansion materials".

Thermal expansion of solids is a physical property that depends on the nature of the interatomic potentials. Thermal expansion of a diatomic molecule can be explained based on the asymmetric shape of a typical interatomic potential well. On a macroscopic scale, normally all dimensions of a solid should increase with rise in temperature and on a microscopic scale we expect the energy of vibrational modes to increase with temperature giving rise to an increase in amplitude of vibrations. The mode Gruneisen parameter (γ_i), relates the fractional change in vibrational frequency to the fractional change in volume.

$$\gamma_i(q) = -((\partial ln\omega_i(q))/\partial lnV)$$

where $\omega_i(q)$ is the frequency of the ith mode vibration of wavevector q in first Brillouin zone and V is the volume. $\omega_i(q)$ is evaluated either using lattice dynamical calculation or high pressure neutron inelastic scattering measurements.

The magnitude of thermal expansion in a material is quantified by its coefficient of thermal expansion. Anomalous thermal expansion materials include those with net low thermal expansion, nearly zero thermal expansion and colossal anisotropic thermal expansion. In this article, we discuss about colossal thermal expansion of KMnAg$_3$(CN)$_6$. Detailed analysis of nature of phonon modes contributing to colossal thermal expansion, negative linear compressibility and pressure induced phase transformations are explained using results obtained from Raman spectroscopy and first principles calculations.

The structure of KMn[Ag(CN)$_2$]$_3$ is closely related to Ag$_3$[Co(CN)$_6$]. The main difference is the inclusion of K+ ions within the cavities of the dicyanometallate framework, lowering the crystal symmetry from P-31m to P312. The trigonal crystal structure of KMnAg$_3$(CN)$_6$ consists of alternating layers of Ag+ and [Mn(CN)$_6$]$^{3-}$ ions, stacked parallel to the trigonal axis and strongly bonded Mn-NC-Ag-CN-Mn linkages running parallel to the <101> directions. The coefficients of thermal expansion of KMn[Ag(CN)$_2$]$_3$ ($\alpha_a = +61 \times 10^{-6}$K^{-1},

$\alpha_c = -60 \times 10^{-6}$K^{-1}) and the linear compressibilities ($\chi_a = +33.2$ TPa^{-1} and $\chi_c = -12$ TPa^{-1}) in the pressure range 0.2-2.2 GPa was shown to be due to wine-rack hinging. It shows a higher magnitude of negative linear compressibility up to 2 GPa without any phase transformation, which makes it more suitable for applications since most machining processes subjects materials to pressures of 1-2 GPa.

KMn[Ag(CN)$_2$]$_3$ crystallizes in a trigonal structure with space group P312 (D$_3{}^1$) with one formula unit in the crystallographic unit cell. The K, Mn, Ag atoms occupy the Wyckoff sites e, a and k respectively; C and N occupy the l sites. Factor group analysis was carried out using Correlation method to obtain the total irreducible representation, $\Gamma_{tot} = 7A_1 + 10A_2 + 17E$, which comprises of internal modes of cyanide ion $\Gamma_{int} = 6A_1 + 6A_2 + 12E$, lattice modes $\Gamma_{ext} = A_1 + 3A_2 + 4E$ and acoustic modes $\Gamma_{acoustic} = A_2 + E$. Therefore, 23 Raman active (7A$_1$+16E) and 25 IR active modes (9A$_2$+16E) are expected from the sample.
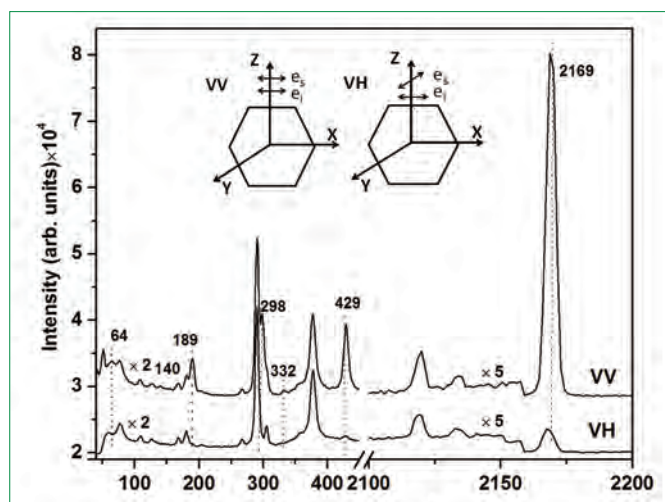

Figure 1: Polarized Raman spectra of KMn[Ag(CN)$_2$]$_3$ in Z(XX)Z′ (VV) and Z(XY)Z′ (VH) scattering geometries at 80 K. Both A$_1$ and E modes appear in VV geometry. The labeled Raman modes that disappeared in the VH geometry are assigned as A$_1$

Single crystals of $KMn[Ag(CN)_2]_3$ were grown by a layering technique. Distinct colorless hexagonal plates were carefully handpicked and observed through a polarizing optical microscope under cross polarized condition. The crystals that appear dark and remain dark through 360° rotation are the ones with their crystallographic c-axis (i.e., the optic axis) perpendicular to the basal plane within the crystal. Such c-oriented single crystals were then used in the polarized Raman measurements to assign the phonon modes. Spectra (Figure 1) were measured at $T = 80$ K in $Z(XX)Z'$ (VV) and $Z(XY)Z'$ (VH) scattering geometries (Porto's notation) where Z is the microscope axis, which is the direction of incident laser, Z is the direction of the scattered signal and X and Y are on the crystal plane.

The allowed symmetry species for c-oriented hexagonal single crystals in $Z(XX)Z'$ (VV) scattering geometry are A_1 and E; in $Z(XY)Z'$ (VH) scattering geometry, only E species is allowed. The bands at 63, 140, 189, 298, 332, 429 and 2168 cm^{-1} are found to appear in the VV but not in the VH geometry and hence they are assigned as A_1 symmetry species. The remaining modes that appear in both the VV and VH geometry are labelled as E modes. The frequencies and their mode assignments are given in Table 1.

We have obtained all expected 7 A_1 modes and only 13 out of 16 E modes. We are thus able to obtain 20 out of the 23 bands in the Raman spectrum. The three bands that could not be observed may be because they are accidentally degenerate with the observed bands, or their Raman scattering cross section could be low.

High pressure Raman experiments were carried out with pressure transmitting medium under hydrostatic condition in symmetric diamond anvil cell. Raman spectra of the sample with pressure transmitting medium in increasing pressure cycles are shown in Figure 2.
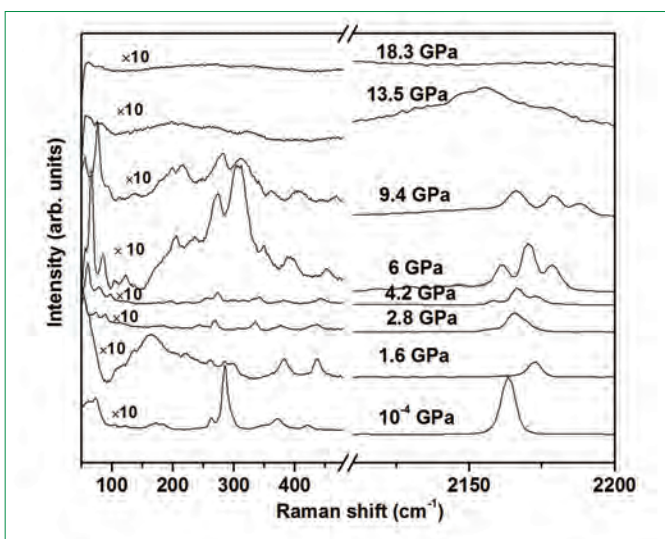

Figure 3: Pressure variation of phonon frequencies of $KMn[Ag(CN)_2]_3$ under hydrostatic conditions

Around 2.8 GPa the intensities of high frequency symmetric stretch mode at 2164 cm^{-1} and some low energy modes around 260 cm^{-1} fall rapidly. The intensities of low energy bands gradually decrease and disappears around 13 GPa indicating possible pressure induced amorphization. Mode frequency versus pressure plot in Figure 3 clearly shows the phase transition at 2.8 GPa and amorphization around 13.5 GPa.

Pressure dependence of Raman bands below 2.8 GPa were used to obtain their corresponding mode Gruneisen parameters. We find that all the γ_i of the Raman modes are positive, which is in accordance with the increasing mode frequencies with increasing pressure. We could not observe soft modes to explain pressure induced transformation using Raman spectroscopy.

First principles calculations of the pressure dependent lattice parameters, phonon spectrum and elastic constants were carried

Figure 2: Raman spectra of $KMn[Ag(CN)_2]_3$ at different pressures under hydrostatic conditions. Dramatic change at 2.8 GPa and amorphization around 13.5 GPa are evident

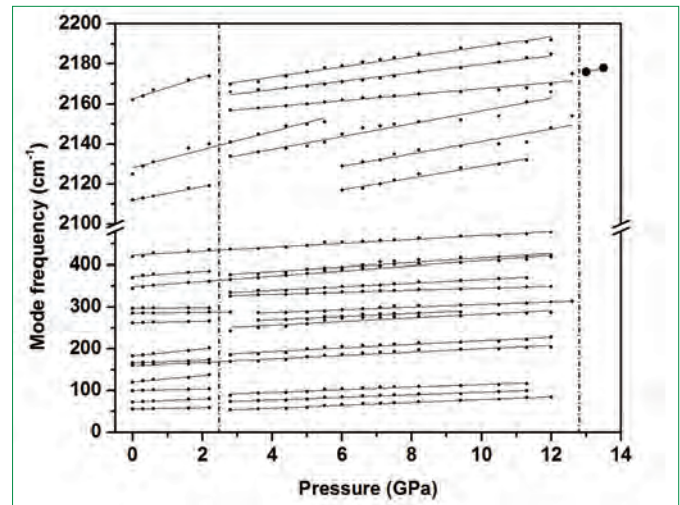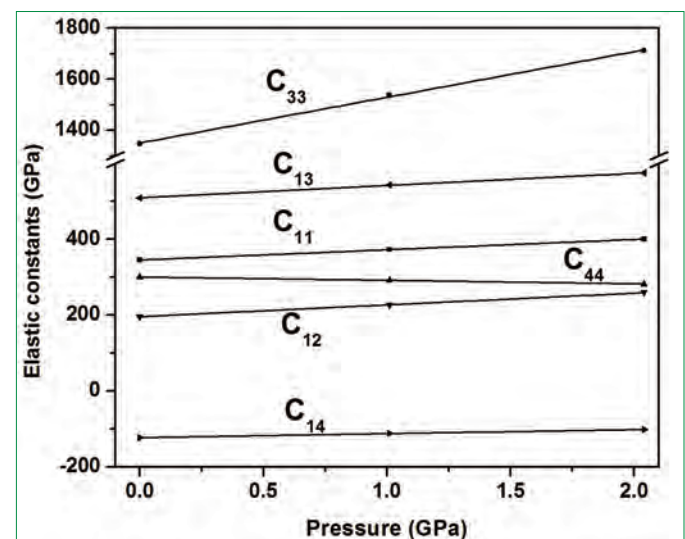Figure 4: Computed pressure dependent elastic constants of $KMn[Ag(CN)_2]_3$. C_{44} shows negative pressure derivatives indicating pressure induced structural instability

Table 1 Comparison of Raman and IR frequencies of $KMn[Ag(CN)_2]_3$ and their mode assignments obtained using Polarised Raman measurements with the computed zone centre phonon frequencies and mode assignments. Mode Gruneisen parameters (γ_i) are also listed. Our DFPT calculations used vDW-DF2 and rPW86 exchange-correlation functional. Mode descriptions are obtained by visualizing atomic displacements using VESTA.

Experimental				DFPT with vDW-DF2 and rPW86			
Raman modes at 80 K (cm-1)	Mode label	IR modes at 300 K (cm-1)	Mode Gruneisen parameter (γ_i)	Zone center modes (cm-1)	Mode Gruneisen parameter (γ_i)	Mode label	Mode description
				38	-0.65	A_2	Ag translation
				49	-0.05	E	Ag translation
				51	2.95	E	Ag translation
60	A_1		0.31	64	2.94	A_1	Ag translation
76	E		0.55	76	1.65	A_2	Mn translation
107	E		0.17	95	1.12	E	K translation
126	E		0.67	125	1.38	E	K+CN translation
140	A_1			144	1.28	A_2	CN translation
168	E	164	0.29	154	1.21	E	CN translation
180	E		0.28				

out using Vienna Ab initio Simulation Package (VASP) and vDW-DF2 and rPW86 functional. Density Functional Perturbation Theory (DFPT) calculations combined with the quasi-harmonic approximation was used to obtain the phonon spectrum and Gruniesen parameters for comparison with experimental values. To compute the mode Gruneisen parameters of $KMn[Ag(CN)_2]_3$, the phonon spectrum was calculated at three different volumes corresponding to pressures 0.0, 1.0 and 2.0 GPa. For the low energy A_2 and E optic modes, calculation gives negative Gruneisen parameter. The computed phonon frequencies and their mode assignments are compared with the corresponding Raman and IR spectroscopy results in Table 1.

To get insight into the large persistent negative linear compressibility of $KMn[Ag(CN)_2]_3$ compared to $Ag_3[Co(CN)_6]$, pressure variation of elastic constants were calculated. The elastic constants were computed using the symmetry-general least-squares method as implemented by VASP. The elastic constants were derived from the strain-stress relationships obtained from six finite distortions of the lattice including contributions of distortions with rigid ions and ionic relaxations.

In Figure 4, it is evident that all the elastic constants increase with pressure except C_{44} which decrease with increasing pressure.
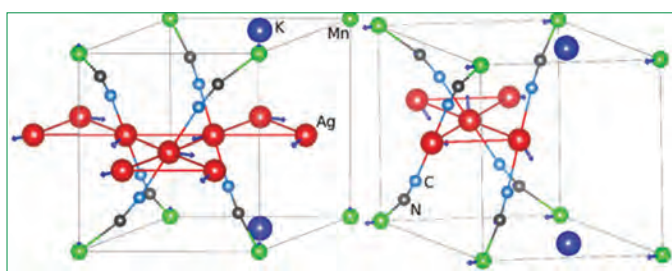

Figure 5: Computed atomic displacements of the low frequency optic modes, (a) the A_2 mode at 38cm-1, (b) the E mode at 49cm-1

Negative pressure derivative of the shear elastic constant C_{44} indicates instability of the lattice, via Born stability criterian. NLC, NTE and pressure induced phase transformations are associated with structural instability determined by negative pressure derivative of elastic constant. This shows that negative linear compressibility of $KMn[Ag(CN)_2]_3$ is driven by lattice instability and anisotropy of the crystal.

In order to understand the pressure induced phase transformation, we analyzed the atomic displacements of all phonon modes of $KMn[Ag(CN)_2]_3$. Figure 5 shows the atomic displacements of the A_2 mode at 38 cm-1 and the E mode at 49 cm-1.

These two low energy optic modes, which show prominent displacement of Ag atoms, are predicted to have negative Gruneisen parameters. Moreover, negative derivative of C_{44} is associated with softening of transverse acoustic modes. Thus, pressure induced phase transformation is caused by transverse acoustic modes and coupled atomic displacement of two soft optic modes.

In summary, linear compressibility and thermal expansion of $KMn[Ag(CN)_2]_3$ are investigated using pressure dependent Raman spectroscopy and DFT calculations. Elastic constants of $KMn[Ag(CN)_2]_3$ shows that the crystal is highly anisotropic, and fulfills the criterion for negative linear compressibility. Negative pressure derivative of C_{44} further indicates instability of the lattice. The pressure induced phase transformation of $KMn[Ag(CN)_2]_3$ observed in our measurements, is due to softening of transverse acoustic mode, which is evident from the negative pressure derivative of C_{44} shear elastic constant, and the A_2 and E low energy soft optic modes.

Reported by
K. Kamali, Materials Science Group

Conference and Meeting Highlights

DAE BRNS Theme Meeting on Plutonium 75
May 23 – 25, 2016

Dr. Sekhar Basu, Chairman AEC and Secretary, DAE inaugurating the DAE BRNS Theme Meeting on Plutonium 75

Towards commemorating the 75th year of the discovery of Pu-239, a DAE BRNS theme meeting titled "Plutonium 75 (Pu75)" was organised during 23 - 25 May 2016 at IGCAR, Kalpakkam. The theme meeting took stock of the excitement and progress in plutonium research and the central role it plays in the Indian Nuclear Power Programme.

The theme meeting was inaugurated by Dr. Sekhar Basu, Chairman, AEC and Secretary, DAE with Dr. R. Chidambaram, Scientific Adviser to the Government of India presiding over the inaugural function. The first plenary lecture was by Dr. David L Clark, Los Alamos National Laboratory, who described details of the discovery of plutonium and the Manhattan Project with the lecture being interspersed with video recordings of Dr. Glenn T Seaborg, the discoverer of plutonium. A number of other invited talks by Indian experts as well as those from abroad on the chemistry, metallurgy and engineering aspects of plutonium, highlighted the progress in plutonium research and technology in our country and elsewhere. A poster session to enable the young researchers to highlight their work was held on the second day.

One of the highlights of the theme meeting was a special session dedicated to the pioneers in plutonium science and technology in the country. Dr. A.N. Prasad, former Director, BARC, Shri S. V. Kumar, former Vice-Chairman, AERB, Dr. D. D. Sood, former Director, Radiochemistry and Isotope Group, BARC, Shri G. R. Balasubramanian, former Director,

Reprocessing Group, IGCAR and Shri M. K. T. Nair, former Director, Waste Management Group, BARC gave a brief account of the various challenges that they had faced when they started the construction of the first reprocessing plant in the country – the Plutonium Plant at BARC, Trombay and also gave a glimpse into the various basic studies that had been conducted in the early sixties on this element at BARC. On the ultimate day after the conclusion of the meet, a special visit to the Reprocessing Facilities at Kalpakkam was arranged to enable them to interact with the current generation of scientists and engineers involved in the design and development of reprocessing facilities. The intense discussion that took place and the transfer of knowledge and advice from the pioneers immensely benefited the current generation.

On the final day of the theme meeting, Shri K. N. Vyas, Director, BARC delivered a special address and handed over prizes to the winners in the poster session. A special session to enable participants from the Indian Industry to discuss their indigenous products generated a lot of interest from the delegates.

The final session of the theme meeting was devoted to Seaborg Memorial Lecture conducted by IANCAS-SRC. Dr. David L Clark, Los Alamos National Laboratory, delivered the lecture titled "Plutonium Science for the 21st Century."

Reported by M. Joseph,
Convener, Pu 75

Dr. R. Chidambaram, Principal Scientific Advisor, Government of India delivering the presidential address

Conference and Meeting Highlights

9th DAE-VIE (Vision for Information Exchange) 2016
Symposium on Emerging Trends in I&C and Computer Systems
June 23-24, 2016

Dr. S. A. V. Satya Murty, Director, IGCAR & GSO, Dr. R. Chidambaram, Principal Scientific Adviser to Government of India, Dr. K. Sivan, Director, Vikram Sarabhai Space Centre, Thiruvananthapuram during the inauguration

The "9th DAE-VIE (Vision for Information Exchange) 2016 Symposium on Emerging Trends in I&C and Computer Systems" was held at Sarabhai Auditorium, IGCAR, Kalpakkam during June 23-24, 2016. Dr. R. Chidambaram, Principal Scientific Adviser to Government of India inaugurated the symposium and released the souvenir. Dr. S. A. V. Satya Murty, Director, IGCAR & GSO delivered the presidential address. Dr. K. Sivan, Director, Vikram Sarabhai Space Centre, Thiruvananthapuram delivered the keynote talk on I&C experiences in space programme. Dr. G. Athithan, Director General (Micro Electronic Devices, Computational Systems & Cyber Systems), DRDO gave a special talk on the second day of the symposium on Cyber Security: Testing & Certification.

DAE-VIE 2016 was organized by Electronics & Instrumentation Group of IGCAR jointly with Kalpakkam

Dr. R. Chidambaram, Principal Scientific Advisor, Government of India, during his visit

chapter of Indian Nuclear Society. The conference was sponsored by Board of Research in Nuclear Sciences.

Seventeen invited talks by eminent experts (fourteen from DAE units, two from DRDO and one from IIT) in areas of I&C for FBR, PHWR. LWR, Information Technology, Information Security, Indigenous microprocessor, High performance computing, cyber security and I&C security were delivered. Sixty nine contributory papers were presented as posters which were grouped in six categories namely Computer Networks & Network Security, PC-based & Embedded Systems, Security Systems, Sensors & Instrumentation, Servers & High Performance Computing and Software Tools, Techniques & Applications. Best poster in each category was selected by a jury of experts and each best poster was awarded a memento and cash prize. The symposium proceedings were published in electronic format and the e-proceedings were given to all participants in a USB flash drive. The technical programme was structured into five sessions with four talks in each session. Leading firms of I&C and computers exhibited their products and also gave technical presentation on their products. More than two hundred and fifty delegates from various units of DAE including aided institutes participated in the symposium. The entire symposium was also streamed live across the IGCAR campus network and also across all DAE units through high speed National Knowledge Network.

Reported by
Organizing Committee, DAE-VIE 2016

Visit of Dignitaries

Shri Vinod Kumar Thakral, IAS, Member Finance, Atomic Energy, Space & Earth Commission with Dr. Arun Kumar Bhaduri, Director IGCAR and senior colleagues during his visit

Shri Vinod Kumar Thakral, IAS, Member Finance, Atomic Energy, Space & Earth Commission visited our Centre on 19 April 2016. During his visit, he visited, the construction site of Fast Reactor Fuel Cycle Facility, Fast Breeder Test Reactor, KAMINI and Hot Cell Facility.

Best Paper/Poster Award

Temperature and Pressure Dependent Phase Transitions of Fast Ion Conductor β'-LiZr$_2$(PO$_4$)$_3$ Studied by Raman Spectroscopy
Ms. K. Kamali and Dr. T. R. Ravindran
DAE-BRNS Symposium CoMPEC (Condensed Matter Physics under Extreme Conditions) held in BARC Mumbai during April 13-16, 2016
Best Poster Award

Black winged Stilt